

# Time-resolved imaging of model astrophysical jets

Theodoros Smponias<sup>1</sup>

*PO box 5, PO 2, Ioannina, Greece*

---

## Abstract

An approximate, time-delayed imaging algorithm is implemented, within existing line-of-sight code. The resulting program acts on hydrocode output data, producing synthetic images, depicting what a model relativistic astrophysical jet looks like to a stationary observer. As part of a suite of imaging and simulation tools, the software is able to visualize a variety of dynamical astrophysical phenomena. A number of tests are performed, in order to confirm code integrity, and to present features of the software. The above demonstrate the potential of the computer program to help interpret astrophysical jet observations.

*Keywords:*

ISM: jets and outflows, stars: winds-outflows, stars: flare, radiation  
mechanisms: general, methods: numerical

*2010 MSC:* 85-08

---

## 1. Introduction

Imaging a relativistically-moving macroscopical object, opens a window to a rather unexpected and even strange world of peculiarities. The basic mandates of Special Relativity, regarding length contraction and time dilation, constitute  
5 a mere beginning, in the quest for comprehension of the actual appearance of a fast-moving object [1, 2, 3, 4, 5]. Looking at the latter, travelling in front of the eye or the telescope, an observer shall *see* the object view affected by a number

---

\*Corresponding author

*Email address:* [t.smponias@hushmail.com](mailto:t.smponias@hushmail.com) (Theodoros Smponias)

of relativistic distortions [6, 7, 8].

In order to simulate the observation of a relativistic astrophysical jet (for  
10 example [9]), a model requires a stationary observer, and a fast-moving gaseous  
mass, comprising both the jet and some of its surrounding matter. The trans-  
formation of electromagnetic emissions, from the jet’s frame of reference to the  
Earth frame, requires performing the Lorentz/Poincaré transform [10, 11, 12, 6].  
Applying the latter transform for imaging purposes, aims to reconstruct what  
15 the observer will actually see, as opposed to what is measured. Relevant to this  
point, [13] argues about the important difference between vision and measure-  
ment in Special Relativity, presenting that difference in a geometrical manner.

Radiation emitted from a jet is therefore subject to relativistic effects [14, 11],  
including time dilation, relativistic aberration and frequency shift, leading col-  
20 lectively to what is known as Doppler boosting and beaming [12, 6, 15]. Aber-  
ration causes the fast-moving object to actually appear *rotated* to a stationary  
observer [2, 3, 16, 6], a phenomenon sometimes called the Terrell-Penrose rota-  
tion.

[17, 18] provide an early computerized attempt to reconstruct a relativis-  
25 tic image, through the eyes of an observer crossing a scene at high velocity.  
[19] demonstrates the importance of the relativistic transform of brightness and  
color. When imaging a jet, these correspond to Doppler boosting and frequency  
shift, respectively. [19] discusses an object that moves at uniform speed across  
the field of view, but is visually large enough for the angle between velocity and  
30 line of sight to vary along the object. Applying the Lorentz transform changes  
brightness and color in a separate manner, for each point of the observed ob-  
ject. [6] improves on such calculations, providing various methods for relativistic  
visualization, in both Special and General relativistic frameworks.

[20] calculate the visual appearance of wireframe relativistic objects, by  
35 mathematically inverting the course of light, from an image point to the emission  
event. They provide expressions that directly describe how a series of objects  
would look like, when moving at high speed, in front of a stationary observer.  
The efficiency of their method is then compared to the increased detail of a

related ray-tracing project [21]. [15] image scenes with a fast observer travel-  
 40 ing through their artificial environment. They also relate their simulations to  
 actual imaging experiments, using the femto-photography technique [22]. Fur-  
 thermore, they introduce a number of additional details into their models, such  
 as camera distortions from traveling at very high speed. [23] present a frame-  
 work, where the subject of relativistic imaging is explored, in a scientifically  
 45 correct and accessible manner.

Even though ray-tracing methods provide excellent quality of relativistic  
 images, they still lack in terms of efficiency, compared to such techniques as  
 polygon rendering [8]. In the current paper, a hybrid relativistic imaging method  
 is presented, whereby time-resolved hydrocode data are being crossed by lines  
 50 of sight (LOS), parallel to each other. Most relativistic effects are directly  
 incorporated, the rest being represented approximately. Some accuracy is thus  
 traded for increased efficiency, allowing for near-real time relativistic imaging of  
 evolving model jets, with modest computing resources.

In the remaining of this paper, the methodology used in the imaging process,  
 55 in order to draw the synthetic image, is presented first (Section 2). We then pro-  
 ceed to briefly describe the new program itself, called RLOS (Relativistic Line Of  
 Sight) (Section 3). Code tests are then provided, whereby imaging is executed  
 repeatedly, with different settings, based on just a few underlying hydrocode  
 runs. Through artificially altering certain parameters in post-processing, imag-  
 60 ing code behaviour is explored, and results are discussed (Section 4). Finally,  
 in Section 5 useful conclusions are drawn from the current work and possible  
 future applications are proposed.

## 2. Implementation

### 2.1. 3-dimensional imaging

65 The 3D setup of RLOS emulates that of its ancestor classical imaging code  
 ([24, 25, 26]). From each pixel of the "imaging" side, of the 3D computational  
 domain (Figure 1), a line of sight (LOS) is drawn, through the imaged volume.

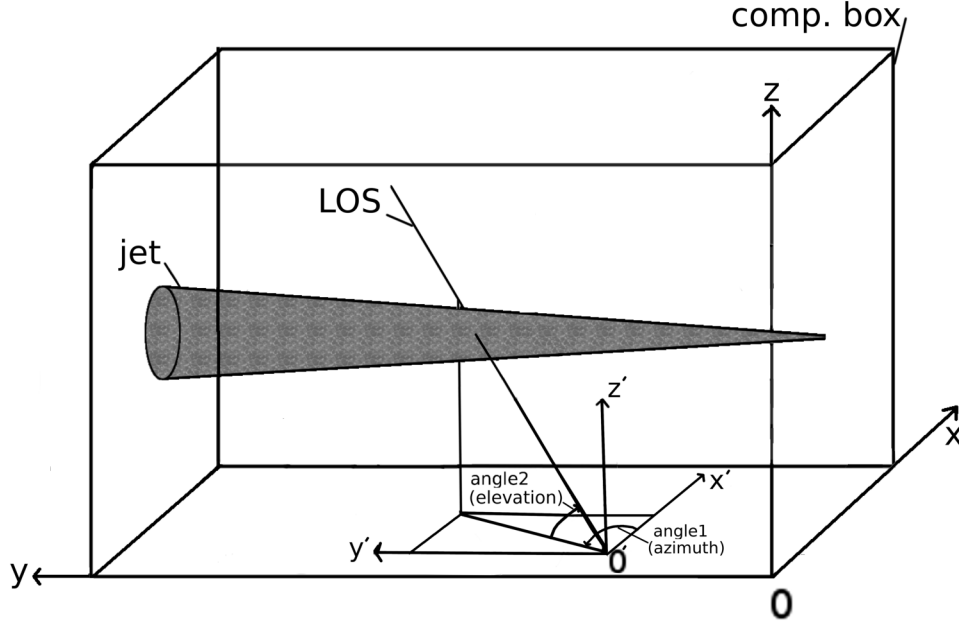


Figure 1: A 3D schematic view, of RLOS applied to a model astrophysical jet. The imaging side of the computational box is the  $yz$  plane, located on the side of the box apparently closer to the reader. Lying on the  $yz$  plane,  $O'$  is the point of origin of a random LOS, with its own dashed coordinate system  $x'y'z'$ . Alternatively, the imaging plane may also lie on the  $xz$  side of the box. The final image is formed on the eye or detector of a fiducial observer, situated at the end of the LOS, through parallel transport.

Along the LOS, the equation of radiative transfer is solved at each cell, using local emission and absorption coefficients. Depending on the situation modelled,  
 70 coefficients may either be calculated directly, or outsourced to another program.

Lines of sight are drawn, starting from a pixel of the  $yz$ -side or  $xz$ -side (either way called the imaging side) of the domain, tracing their way along the given direction (Figures 1 and 2), until they reach a length of  $\sqrt{(x_{max}^2 + y_{max}^2 + z_{max}^2)}$ , where  $x_{max}, y_{max}, z_{max}$  are the dimensions, in cells, of the computational do-  
 75 main. In practice, on reaching the ends of the domain a LOS calculation halts, therefore some LOS's end up shorter than others. The above process is repeated within a 2D loop, running over the imaging plane, each LOS corresponding to a single pixel of the final synthetic image. Along a LOS, no sideways scattering

is considered.

80 A model astrophysical system may be inserted into RLOS directly, for example forming a 'conical' jet setup [27]. Alternatively, data output from a hydrocode may be employed, which is the case in the current paper, using PLUTO [28].

## 2.2. Time-resolved imaging

### 85 2.2.1. Accessing 4-dimensional data

The finite nature of the speed of light affects the appearance of a fast-moving object in a crucial manner. Consequently, drawing a relativistic image of an astrophysical system, necessitates the availability of information regarding not only its spatial properties, but its temporal evolution as well. In our case, 90 when executing the hydrocode, before running RLOS, we adjust the temporal density of snapshots, to be saved to disk at regular intervals. The smaller those intervals, the better the temporal resolution of hydrocode data. A series of snapshots shall then be loaded to RAM by RLOS, which therefore requires a multiple quantity of memory, in order to run properly, than the hydrocode 95 itself. Time is measured in simulation time units, which are read by PLUTO's attached 'pload.pro' routine, which loads data into RLOS.

The total time span available to a LOS,  $\Delta t_{LOS(total)} = t_{(last-shot)} - t_{(first-shot)}$ <sup>1</sup> (as measured in simulation time units, *not* merely in number of snapshots), should be preset to be larger than the light crossing time of the 100 model system, at the selected LOS angle settings. Documenting the model jet evolution generally requires hydrocode data saves to be rather dense in time, especially for fast-changing flows. On the other hand, a lower temporal resolution will probably suffice for a steadier, slower-paced flow.

---

<sup>1</sup>Not to be confused with the interval  $\Delta t_{shot}$  between *successive* snapshots

### 2.2.2. Traversing the 4D arrays

105 *Introduction.* A series of hydrocode snapshots are loaded to RAM, populating the elements of 4-dimensional (4D) arrays. From a *temporal* point of view, we begin from the simulation time corresponding to the first of the loaded snapshots, called shotmin. From a *spatial* point of view, we start at the first point of the imaging plane, which is a side of the computational box (Figure 1).  
110 As the calculation advances, in 3D space, along the LOS being drawn (Figure 2), the algorithm keeps checking whether to jump to a new *temporal* slice, while staying 'on target' in 3D (Figure 3). Consequently, the LOS advances in time, through data (Figure 4), by accessing successive instants from the 4D data arrays.

115 *Time-resolved imaging calculations.* For every LOS, there is a point of origin (POO), located on the "imaging side" of the computational grid (Figure 1). That point, addressed in the code as (nx10, ny10, nz10) and here as  $O'$ , is the beginning of the LOS's axes  $x'$ ,  $y'$ ,  $z'$ , parallel to  $x$ ,  $y$ ,  $z$  respectively. A 2D loop covers the imaging surface, the POO successively locating itself at each of the  
120 latter's points.

As we progress along a LOS, a record is kept of where we are, in 3D space. This record comprises the LOS's own integer coordinates, rc, uc, and cc, measured, in cells, from its POO. The above symbols stand for right-current, up-current and climb-current, representing the current LOS advance in the  $x'$ ,  $y'$   
125 and  $z'$  axes, respectively (Figures 1 and 2). The current ray position is then (nx10+rc, ny10+uc, nz10+cc).

A timer variable, curtime (standing for current LOS time), is introduced for each LOS, recording the duration of insofar ray travel along the LOS. The aforementioned timer is preset at the beginning of each LOS, to the hydrocode  
130 time of the first loaded data snapshot.

We then proceed to calculate the current length of the LOS

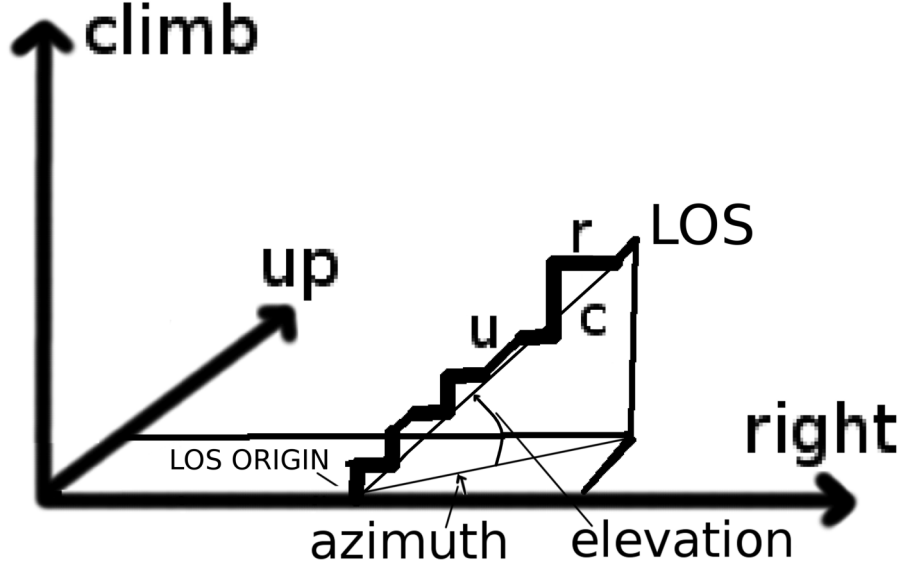


Figure 2: A schematic of the spatial propagation of the line of sight (LOS) through the 3D Cartesian computational grid. In the discrete grid, according to the design of the algorithm, there are 3 available directions to be taken at each step along the LOS: *right*, *up* and *climb*. These correspond to x, y and z, respectively. During propagation, the LOS 'tries' to follow its given direction, as defined by the two angles of azimuth and elevation. More specifically, every two steps a decision is first made on azimuth, either right or up. Then, for elevation, it is either climb, or another azimuth decision. In the Figure, along the LOS, horizontal steps point to the 'right' direction. Diagonal steps represent going 'up', while vertical ones constitute 'climb' steps.

$$l_{los(current)} = [(dlr * (nx1current - nx10))^2 + (dlu * (ny1current - ny10))^2 + (dlc * (nz1current - nz10))^2]^{1/2} \quad (1)$$

where the LOS length is measured in cell length units and

$$nx1current = nx10 + rc, \quad ny1current = ny10 + uc, \quad nz1current = nz10 + cc \quad (2)$$

Along the x, y and z directions, dlc, dlu, dlr are the respective *normalized* hydrocode cartesian cell lengths. Their values are usually unity, or close to unity, as set in the hydrocode by the user, and RLOS requires them fixed, meaning only homogeneous grids are currently supported. Furthermore, if the

135

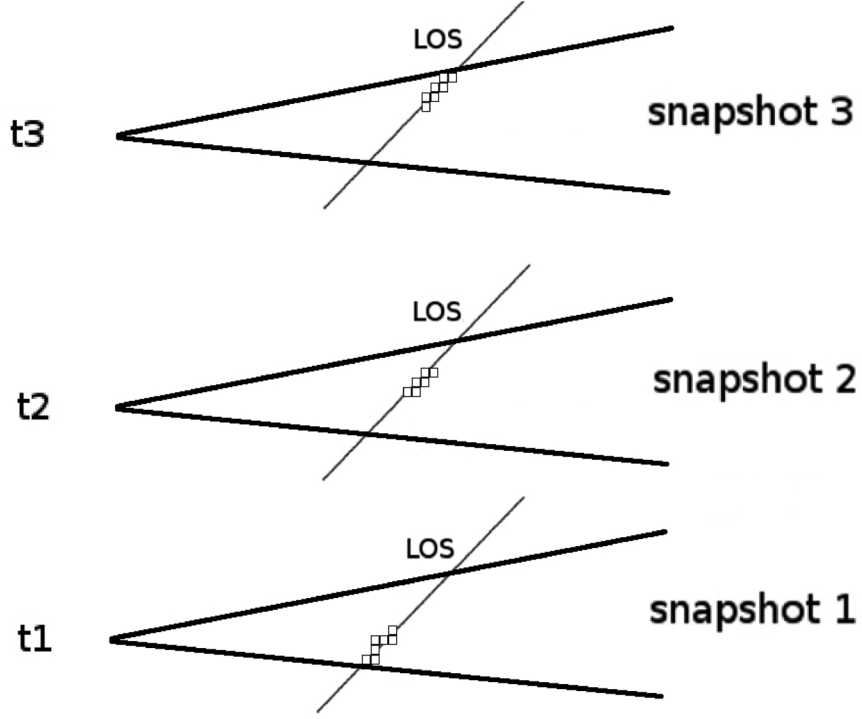


Figure 3: Three successive instants of a line of sight traversing a jet. At regular intervals, we jump to a new 3D slice of a 4D spacetime array, obtaining a discrete approximation of the time continuum, in the form of hydrocode snapshots.

hydrocode grid is read, by pload, at a reduced resolution, then RLOS cell sizes are automatically adjusted accordingly.

We can finally write

$$l_{los(current)} = [((dlr * rc)^2) + ((dlu * uc)^2) + ((dlc * cc)^2)]^{1/2} \quad (3)$$

We then proceed to calculate curtime, the current hydro simulation time of the light ray along the LOS.

$$curtime = l_{los(current)} / c_{light} + t_{0(LOS)}. \quad (4)$$

$t_{0(LOS)}$  is the timestamp of the first loaded snapshot, when the LOS begins to be drawn, from its point of origin, and  $c_{light}$  is the speed of light, in cells per simulation second.

When curtime exceeds the next snapshot's timetag, the algorithm switches to drawing the LOS through the 3D volume of the next available snapshot



(Figure 3). We keep moving along the same LOS in 3-D space, but we have just shifted to a new instant in the time records of the hydrocode. The above  
145 temporal shift is repeated as many times as required by the relevant criterion along the LOS, until the spatial end of the LOS.

### 2.2.3. Aiming the line of sight

The direction of a LOS in 3D space is defined by the two angles of azimuth (angle 1) and elevation (angle 2) (Figure 1), where the plane of angle 1 is the  
150  $x'y'$  plane, parallel to  $xy$ . For a jet parallel to the  $y$  axis, the angle between the local jet matter velocity  $\vec{u}$ , and the LOS,  $\text{losu} = (\widehat{LOS}, \vec{u})$ , is usually small, when angle 1 approaches 90 degrees, and vice versa (Figure 5). As is well known [11], the angle  $\text{losu}$  affects the relativistic emission calculations.

Short of jet precession occurring, the plane of angle 2 (elevation) is largely  
155 perpendicular to the jet when angle 1 is zero, while it is roughly parallel to the jet when angle 1 is 90 degrees. Usually, the jet bears an approximate cylindrical symmetry, meaning that for a small angle 1, by varying angle 2, we 'rotate' the view around the jet axis, producing similar intensities throughout the way. In summary, for a jet moving along the  $y$  axis, the smaller angle 1 is, the less  
160 difference varying angle 2 makes.

On the other hand, for angle 1 nearing  $\pi/2$ , varying angle 2 rotates the view within a plane approximately parallel to the jet, resulting to considerable differences. Consequently, the larger angle 1 is, the stronger the effect, on the synthetic image, from changing angle 2.

### 2.3. Relativistic Effects

The main effects of the Lorentz/Poincaré transform on the emission from a relativistic object [6], specifically applied to an astrophysical jet, are relativistic aberration, time dilation and frequency shift [10, 11, 29, 30].

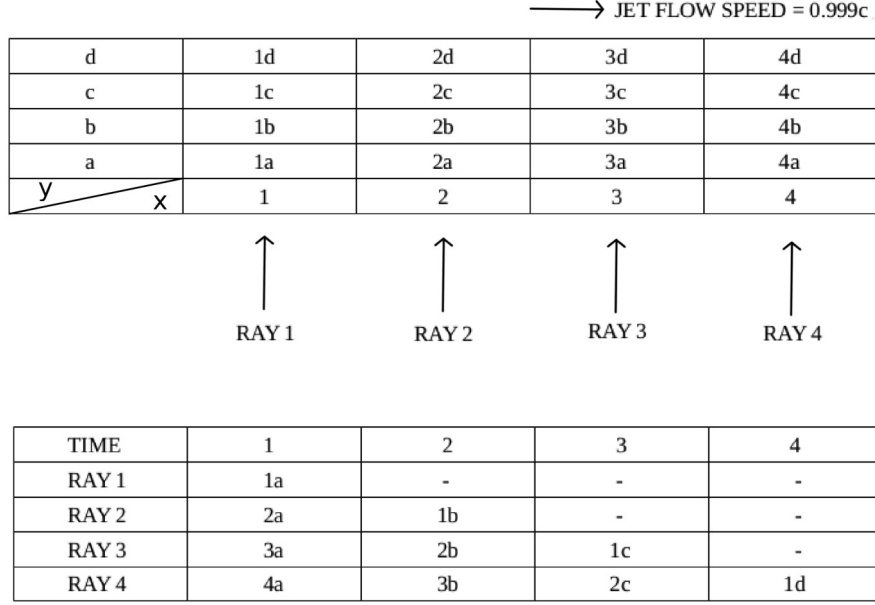


Figure 4: Simultaneous advance, in both space (2D) and time, of a few lines of sight. Top half depicts the spatial situation at  $t=1$ . Sixteen jet matter portions currently occupy this mini 4 by 4 grid. Each piece of matter is named after its position at  $t=1$  and retains that name as it moves along. The bottom half shows how the situation evolves as time marches on, with light rays meeting different jet segments that cross their path. A dash means a light ray meeting jet matter other than the above, or nothing at all.

### 2.3.1. Lorentz factor

170 The Lorentz factor for a hydrocode cell is [11]

$$\Gamma_{Lorentz} = \frac{1}{\sqrt{1-u^2}} \quad (5)$$

where

$$u = \sqrt{u_x^2 + u_y^2 + u_z^2} \leq 1 \quad (6)$$

is the value of the local velocity  $\vec{u} = (u_x, u_y, u_z)$ , in units of the speed of light.

### 2.3.2. Doppler factor calculation

In the effect of Doppler boosting (DB), radiation is either boosted or de-boosted, depending on the angle  $\text{losu}$ , between the direction of the LOS and  $\vec{u}$ . The closer we are to observing the jet head-on (average  $\text{losu}$  getting smaller),

the stronger the boosting becomes. In addition, the higher the jet speed, the narrower and stronger the cell boost cones around the jet head direction. On the other hand, outside cell boost cones, *de*-boosting occurs, that is to say the higher the velocity is, the weaker the signal becomes. The Doppler factor D is obtained from the expression:

$$D = \frac{\sqrt{1-u^2}}{(1-u * \cos(\text{losu}))} \quad (7)$$

The cosine of angle losu is calculated in the following manner:

Let us define a fiducial unitary vector ( $\vec{LOS}$ ) = ( $lx_1, lx_2, lx_3$ ), with ( $LOS$ ) =  $\sqrt{lx_1^2 + lx_2^2 + lx_3^2} = 1$ , pointing along the preset direction of the LOS's. In the following,  $\phi_1$  and  $\phi_2$  represent angle 1 and angle 2, respectively.

$$lx_1 = \cos(\phi_1)\cos(\phi_2), \quad lx_2 = \sin(\phi_1)\cos(\phi_2), \quad lx_3 = \sin(\phi_2) \quad (8)$$

where both angles are known, and are fixed for parallel lines of sight. We now have

$$\vec{LOS} * \vec{u} = (LOS) * u * \cos(\widehat{\vec{LOS}, \vec{u}}). \quad (9)$$

Alternatively,

$$\vec{LOS} * \vec{u} = lx_1 * u_x + lx_2 * u_y + lx_3 * u_z \quad (10)$$

Therefore, from equations 9 and 10, we have

$$\cos(\widehat{\vec{LOS}, \vec{u}}) = \frac{lx_1 * u_x + lx_2 * u_y + lx_3 * u_z}{(LOS) * u} \quad (11)$$

Since (LOS)=1, and from equations 6 and 11, we obtain

$$\cos(\widehat{\vec{LOS}, \vec{u}}) = \frac{lx_1 * u_x + lx_2 * u_y + lx_3 * u_z}{\sqrt{(u_x^2 + u_y^2 + u_z^2)}} \quad (12)$$

Where  $lx_1$ ,  $lx_2$  and  $lx_3$  are known from equations 8. In practice, a miniscule number is added to the denominator of equation 12, in order to avoid possible division by zero, in case  $u=0$ . The above calculation allows the assignment of a Doppler boosting factor, through equations 6, 7 and 12, to each discrete emission event along a line of sight.

### 2.3.3. Doppler boosting

Earth frame jet emissivity  $S_{obs}$  can be expressed [11, 10] as

$$S_{obs} = S_{jet} D^{3+\alpha} \quad (13)$$

180 where  $\alpha$  is the spectral index. The exponent  $(3+\alpha)$  in the above can be broken down into different contributions from separate effects. Two units come from the aberration of light, one from the relativistic dilation of time and  $\alpha$  from the effect of frequency shift, while for a continuous optically thin jet a D factor is lost [10].

*Power-law frequency shift.* Radiation emitted at a given frequency, from fast-moving jet matter, is taken to be Doppler shifted in frequency

$$f_{obs} = f_{calc} D \quad (14)$$

where  $f_{obs}$  is the observed frequency and  $f_{calc}$  is the frequency used in the emission calculations, performed in the jet frame of reference [11]. In order to accomodate for the shift, a power-law spectrum, falling off with frequency, is employed

$$S_f \propto f^{-\alpha} \quad (15)$$

185 with  $\alpha$  assumed, as an approximation, to take the value of  $\alpha = 2.0$ , generally referring to the optically thin region of the jet. For  $D \geq 1$ , emission is calculated at a frequency lower than the observed, resulting to a higher intensity, since the spectrum employed generally decreases with frequency.

*Alternative frequency shift.* RLOS may include different emission dependencies on frequency, where we calculate intensity at  $f_{calc}$  and observe that at  $f_{obs}$ . 190 At the moment, the above is included only as a quantitative indicator, where intensity may be optionally multiplied by the square of the ratio  $f_{calc}/f_{obs} = 1/D^2$ , partially negating the effect of Doppler boosting.

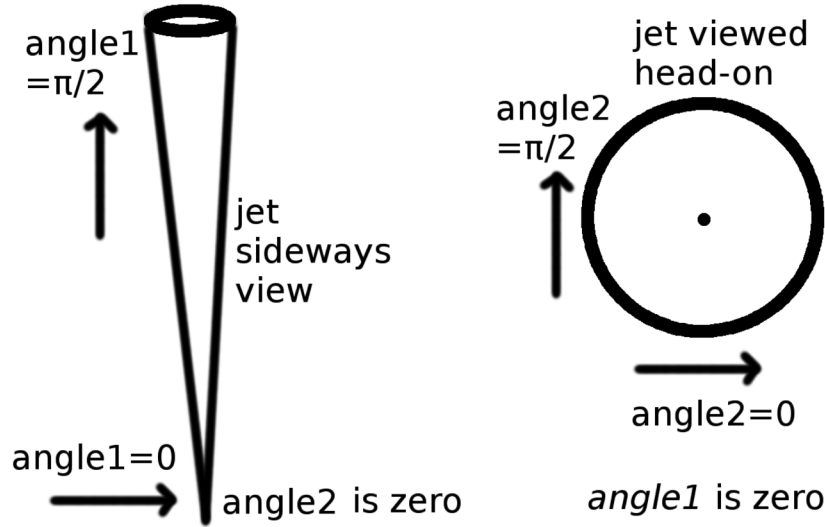


Figure 5: The geometric arrangement with regard to the viewing angles in the model, for the special cases of  $\text{angle2} = 0$  (left) and  $\text{angle1} = 0$  (right). For each sub-case, the arrow shows the direction of the LOS, which is different than the reader's direction of view.

*Aberration-searchlight effect.* Relativistic aberration changes the perceived direction of light, when transforming between the jet frame and the earth frame,  
 195 'tilting rays', emanating from the jet, towards its head area. The resulting path of light is nevertheless *measured* to be identical in both frames of reference, as shown in [6], section 4.6.1. As an approximation, we opted to forgo this effect geometrically, only employing straight lines of sight. In order to compensate  
 200 for the above simplification, two Doppler factors, representing aberration, are employed in the Doppler beaming formula. Instead of focusing sidereal rays to the front, while diluting those to the side, we simply multiply the intensity of each emission event, by the event's own  $D^2$ . For reasons of efficiency, this takes place for each cell, for each snapshot, before the main loop. Cell emission  
 205 along a ray *within* the cell's boost cone, is then reinforced accordingly, while if *outside* the cone it is weakened, an approximation that reduces the complexity of code setup (all rays are parallel) and also its computational load. Depending on the local velocity value and direction, successive or neighbouring cells may

have totally different boost cones.

210 *Time dilation.* Time dilation contributes one D factor to the emission result.

#### 2.4. Testing parameters

Certain parameters, that facilitate testing RLOS, are presented here.

##### 2.4.1. The clight parameter

Let us consider a 4D array, comprising a succession of hydrocode snapshots.  
 215 The LOS traversing those data, moves at a speed of clight cells per time unit.  
 When we artificially adjust clight to a lower value [31, 23], then the algorithm  
 jumps to a new snapshot after spatially advancing through fewer cells. A slower  
 LOS advances farther in time while crossing a given distance through the jet,  
 allowing for a detailed study of the time-jumping algorithm. On the other  
 220 hand, setting clight to a very high value leads to a single shot image, as we  
 never advance to a further temporal slice.

In the current work, hydrocode runs employ the following scaling

$$L_{sim} = 10^{10} cm, u_{sim} = 3 \cdot 10^{10} \frac{cm}{s}, \rho_{sim} = 1.67 \cdot 10^{-24} \frac{g}{cm^3} t_{sim} = \frac{L_{sim}}{u_{sim}} = \frac{1}{3} s$$

$$B_{sim} = \sqrt{4\pi\rho_{sim}u_{sim}^2} = \sqrt{4\pi \cdot 1.67 \cdot 10^{-24} \cdot 9 \cdot 10^{20}} \simeq 0.137 G.$$

(16)

where  $t_{sim}$  is the hydrocode time unit,  $u_{sim}$  is the speed of light and  $l_{sim}$  is the  
 hydrocode length unit. The cell length in the simulations is conveniently setup  
 to the value of one model length unit  $l_{cell} = L_{sim}$ , leading to an intrinsic clight  
 225 value of 1, verifying clight as the speed of light in cells/s. When preparing the  
 hydrocode run, the time span, in simulation seconds, between data snapshots,  
 should optimally be set, to  $l_{LOS}/(n \cdot clight)$ .  $l$  is the LOS length, in *cells* and  $n$   
 is the desired number of snapshots to cover the imaged timespan. If we employ  
 the parameter sfactor, pload's shrink factor, imaging voxels are enlarged and  
 230 the calculated value of clight shrinks accordingly. Overall accuracy then suffers  
 somewhat, and shrinking the grid should be used only as a preview.

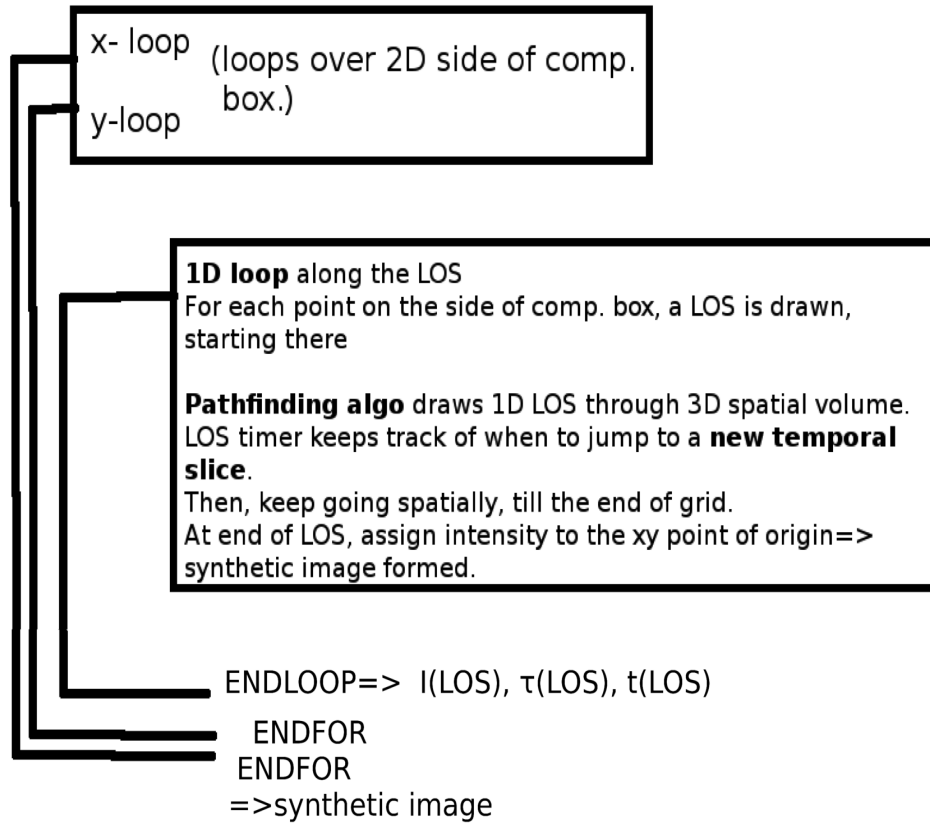


Figure 6: A simplified flow diagram depicting the basic logical structure of RLOS imaging code. The synthetic image's xy loops here correspond to either the yz or the xz side plane of the computational box.

The value of *clight* may be manually overridden within RLOS, yet altering *clight* only affects the light ray speed, not the speed of matter. Consequently, overriding *clight* does not affect the relativistic emission calculations (like tweak-speed does, Section 2.4.2). An altered *clight* is merely an artifice, introduced in post processing, in order to explore the effect of using more, or less, temporal slices in the final image.

#### 2.4.2. The speed tweak parameter

A test is introduced, where matter velocity is multiplied, on a global scale, by a 'speed tweak' factor. This offers a quick way to observe the impact, on

the synthetic image, of altering the hydrodynamic speed in post-processing, for the same simulation run. The natural value of tweakspeed is 1. At low tweak speed factors (less than 1) the effects, on the final image, of both DB and FS, are reduced, and vice versa. The maximum for tweakspeed is  $c/u_{(max)}$ , above  
 245 which velocities higher than  $c$  are artificially created in the grid.

#### 2.4.3. The FS switch

After the hydrodata are loaded, a global operation calculates, for each cell, a jet frame frequency  $f_{calc}$ , from the common observing one  $f_{obs}$ :  $f_{calc} = f_{obs}/D$ . The frequency shift (FS) switch selects between using the local  $f_{calc}$  or the global  
 250  $f_{obs}$  in the emission calculations. In this paper, a boost of  $D^\alpha$  already simulates an *implied* dependence on frequency. The FS facility allows for a user-defined spectrum to be introduced, such as from synchotron emission ([27]).

#### 2.4.4. The DB switch

The DB switch offers the option of using the Doppler boosting effect, in the  
 255 form of  $D^{3+\alpha}$ .

#### 2.4.5. An example

As an example, we distinguish four different combinations of DB and FS. Emissivity is measured in arbitrary units, common for all cases.

1. Both DB and FS turned on.

$$emiss_{FD} \propto \rho D^{3+\alpha} \left( \frac{f_{calc}}{f_{obs}} \right)^2 = \rho D^{1+\alpha} \quad (17)$$

- 260 2. DB turned on, FS turned off.

$$emiss_D \propto \rho D^{3+\alpha} \quad (18)$$

3. DB turned off, FS turned on.

$$emiss_F \propto \rho \left( \frac{f_{calc}}{f_{obs}} \right)^2 = \frac{\rho}{D^2}, \quad (19)$$

4. DB turned off, FS turned off.

$$emiss_{none} \propto \rho \quad (20)$$



### 3. Description of RLOS

RLOS is written for the IDL or the GDL programming languages, and is  
265 released under the LGPL licence. It replaces its classical ancestor, as part of  
a suite of simulation and visualization programs that study astrophysical jets,  
in a perceived numerical laboratory. The latter combined approach employs  
a hydrocode, LOS code, a visualization package, and a number of in-house  
gamma-ray [25, 26] and neutrino emission calculation programs [32, 33]. The  
270 addition of RLOS to the above software suite, aims to reinforce the realism  
of the imaging part of the calculations. Finally, the modular structure of the  
program facilitates the inclusion of more physical effects in the future.

RLOS is organized in two outer spatial loops, running over the imaging plane  
and an inner 1-dimensional spatial loop, advancing in pairs of steps, one for each  
275 angle, running over the length of a LOS. At the innermost lies a *conditional*  
temporal loop, running over the hydro data time span. The basic structure  
of the algorithm can be seen in Figure 6. Since much of the calculation load  
is global, it is performed, where feasible, before the loops, in array-oriented  
operations, in order to improve performance.

### 280 4. Results and discussion

#### 4.1. Model setup

In this Section, RLOS is tested under different circumstances, based on just  
a few underlying hydrocode runs. This way, the effect of altering each parameter  
on the final synthetic image is examined.

285 An intermittent model jet, representing a microquasar system, injected at  
 $u_{jet} = 0.26c, 0.6c$  or  $0.8c$  is studied with the RMHD setup of the PLUTO  
hydrocode, at a uniform grid resolution of  $60 \times 100 \times 60$ . In all of the model  
runs the same initial jet density of  $10^{10}$  protons/cm<sup>3</sup> is used, 10 times less than  
the maximum surrounding gas density. Winds comprise an accretion disk wind  
290 construct and a stellar wind, which falls off away from the companion star,  
located off-grid at (400, 0, 400), while the jet is threaded by a strong confining

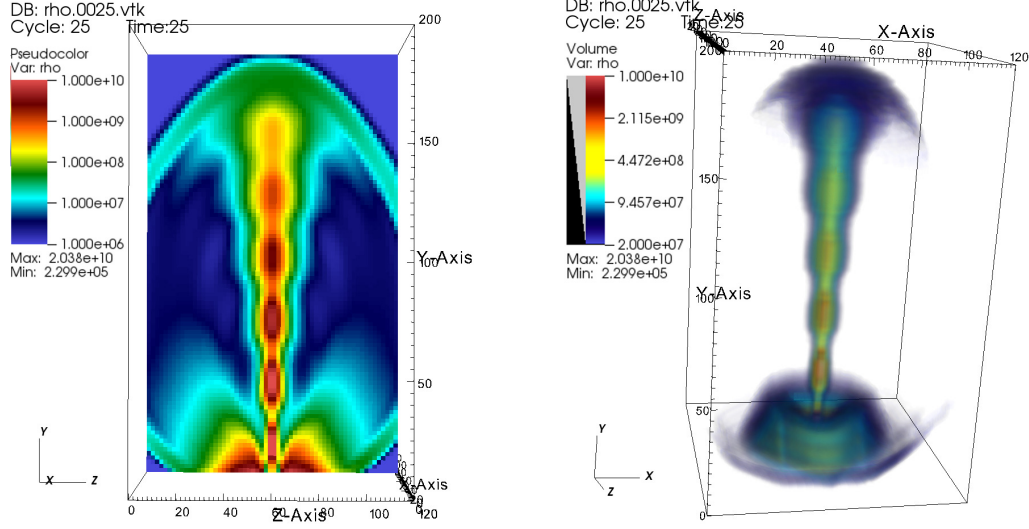


Figure 7: Snapshot 25 of the  $u=0.6c$  hydrocode run, corresponding to a model time of  $t=375$  ( $25 \times 15$ ), depicting the density. We can see the jet front reaching the end of the grid, having advanced though increasingly lighter surrounding winds, after crossing the simplified accretion disk wind construct. On the left is presented a slice cut through the data and on the right a 3-dimensional density plot. Image produced with VisIt.

toroidal magnetic field of  $B=400$  simulation units. Blobs are emitted during the first 1.5 out of every 10 time units (simulation seconds), for both the  $u=0.26c$  and the  $u=0.8c$  models, while for the  $u=0.6c$  case, the jet is on during the first 5 out of every 50 time units. The simulations were run until at least  $t = 750$ , saving a data snapshot every 15 time units. Taken from the  $u=0.6c$  model run, a snapshot of density is shown in Figure 7, in both 2D and 3D, where we can see the magnetically collimated sequence of plasmoids advancing through surrounding winds.

RLOS was then run, based on the above hydrocode data, with  $\text{sfactor}=1$  for the plod shrink factor. In general, the imaging process may or may not use all snapshots available to it, depending on the light crossing time of its model segment (potentially adjusted through the  $\text{clight}$  parameter). Trying to read more snapshots than loaded corrupts the hydrocode time array, called  $T$ , resulting to errors.

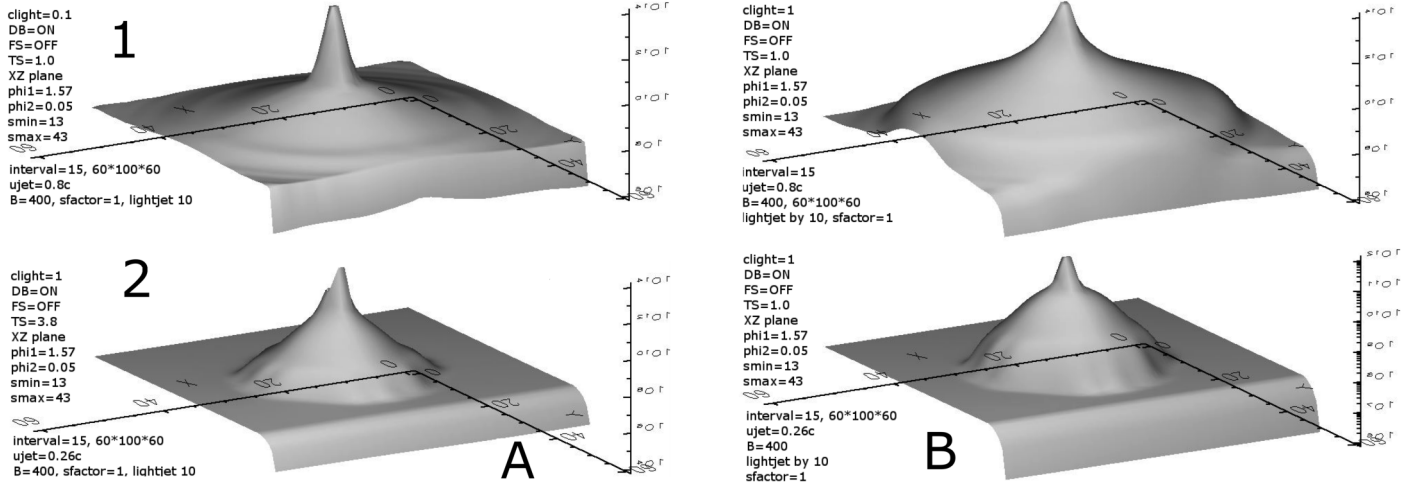


Figure 8: First and only part of the first batch of the results.

The synthetic images are *logarithmic* plots of intensity. Emissivity is proportional to matter density, using the same arbitrary scale everywhere. Doppler boosted intensity is proportional to  $D^{3+a}$ , for an optically thin jet comprising a series of plasmoids [10]. No self absorption is employed, even though the feature

310

Later on in this Section, comparisons between different runs of the imaging code are presented, demonstrating the effect of altering a given parameter, on the synthetic image. Each run is identified by both its information tag and by a chessboard-like 2D pair of alpha-numerical coordinates, referring to the

315

We now define the following correspondences: Process 1 page 1 is shown in Figure 8, process 2 page 1 in Figure 9, process 2 page 2 in Figure 10, process 2 page 3 in Figure 11, process 3 page 1 in Figure 12, process 3 page 2 in Figure 13, process 4 page 1 in Figure 14.

320

The synthetic images are referred to as follows: (process or 'batch' number, page or 'part' number, alphanumeric coordinate, imaging data). For example,

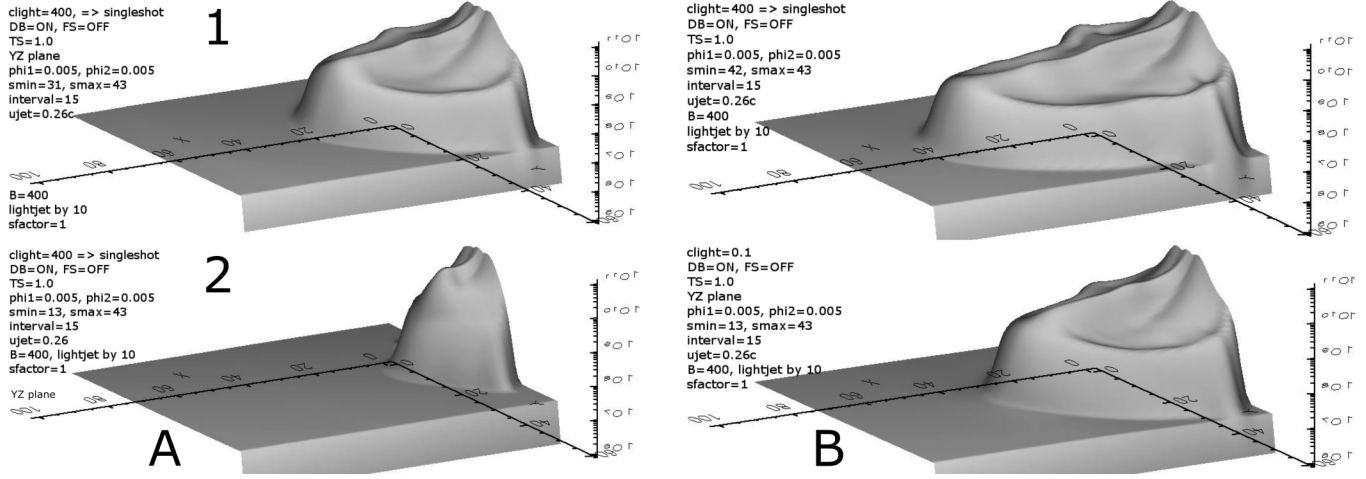


Figure 9: First part of the second batch of the results.

(1, 1, 1A, data) means process 1, page 1, line 1, column A. The 'data' part contains values of certain imaging parameters, *ts* standing for tweakspeed, *clight* for itself, *a1* for angle 1 and *a2* for angle 2, both measured in radians, *DB* for the Doppler boosting switch and *FS* for the frequency shift switch, *smin*/*smax* are the first and last among the snapshots employed, the imaging plane (*xz* or *yz*), and  $u_{jet}$  is the nominal injection speed of the jet matter. In the annotated Figures of the results, *phi1* and *phi2* are the two angles of azimuth and elevation respectively, and *snapshotmax* is the maximum snapshot count of a LOS. Each of the following subsections describes the effects that changing a certain parameter has on the synthetic image.

#### 4.2. Viewing angles

*A pair.* (process2, page2, 1B, *ts*=1.0, *clight*=1, *a1*=0.59, *a2*=0.005, *DB*=on, *FS*=off, *smin*=37, *smax*=43,  $u_{jet}$ =0.26c, *YZ*) vs  
 (process2, page3, 1A, *ts*=1.0, *clight*=1, *a1*=0.005, *a2*=0.005, *DB*=on, *FS*=off, *smin*=37, *smax*=43,  $u_{jet}$ =0.26c, *YZ*)

Comment: When angle 1 is small, the LOS is nearly perpendicular to the

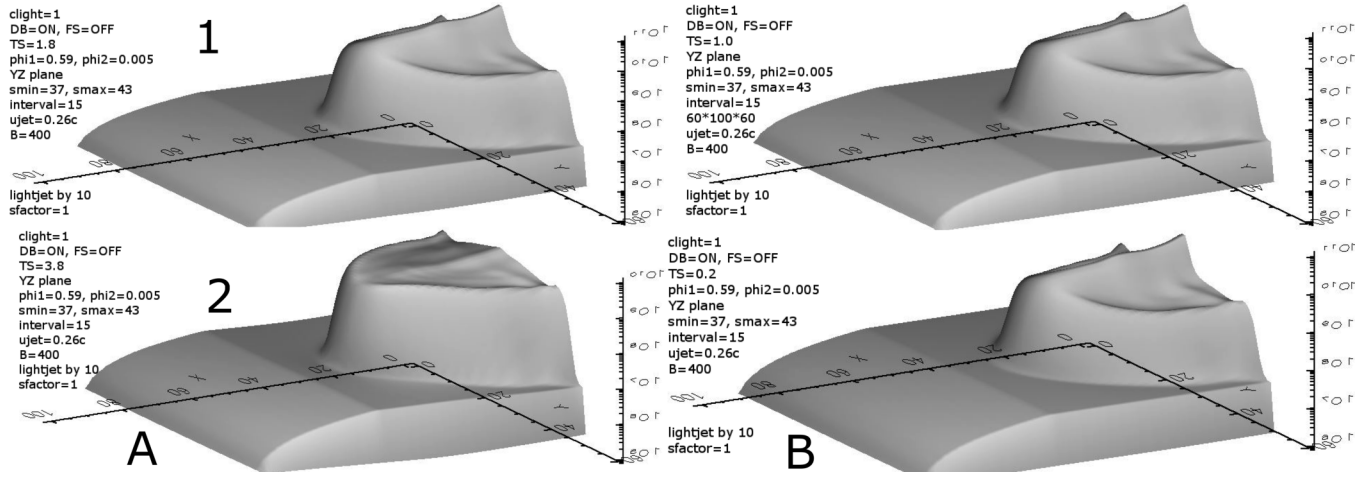


Figure 10: Second part of the second batch of the results.

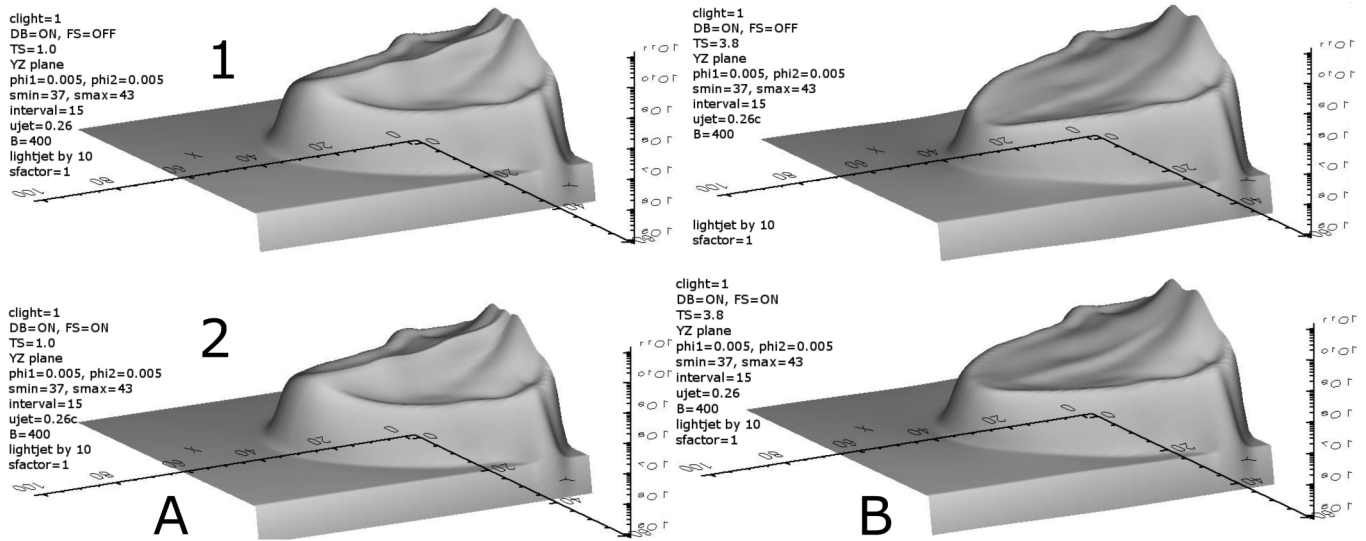


Figure 11: Third part of the second batch of the results.

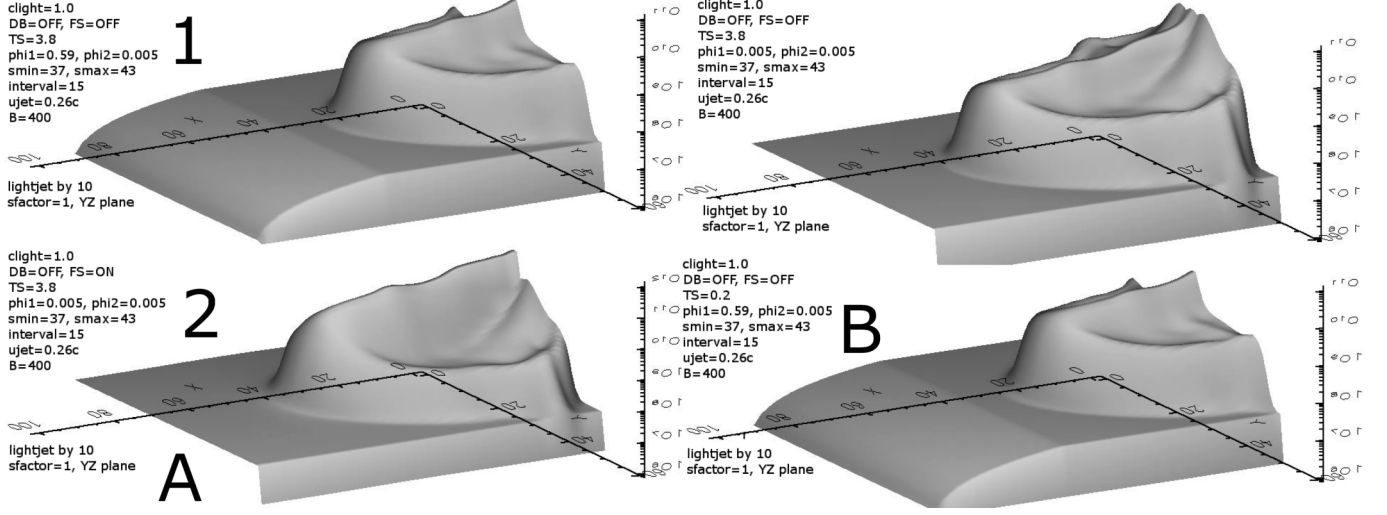


Figure 12: First part of the third batch of the results.

jet, depicting the object clearly. The larger angle 1 becomes, the more off target the image is created. If angle1 approaches  $\pi/2$ , the jet is observed nearly along its axis. Then, it is time to draw the image on the XZ imaging plane.

*A pair.* (process4, page1, 1A, ts=1.0, clight=1, a1=0.45, a2=0.005, DB=on, FS=off, smin=18, smax=23,  $u_{jet}=0.6c$ , YZ) vs (process4, page1, 2A, ts=1.0, clight=1, a1=0.45, a2=0.35, DB=on, FS=off, smin=18, smax=23,  $u_{jet}=0.6c$ , YZ)

Comment: Angle 2 is varied here, at a large angle 1. Consequently, the view is rotated, within the plane of elevation, around a direction non-parallel to the jet, resulting to quite large differences between the two images (Section 2.2.3).

*A pair.* (process4, page1, 1B, ts=1.0, clight=1, a1=0.005, a2=0.35, DB=on, FS=off, smin=18, smax=23,  $u_{jet}=0.6c$ , YZ) vs (process4, page1, 2B, ts=1.0, clight=1, a1=0.005, a2=0.005, DB=on, FS=off, smin=18, smax=23,  $u_{jet}=0.6c$ , YZ)

Comment: Angle 2 is varied here, this time at a *small* angle 1. As a result, the view is rotated around a direction nearly parallel to the jet, resulting to

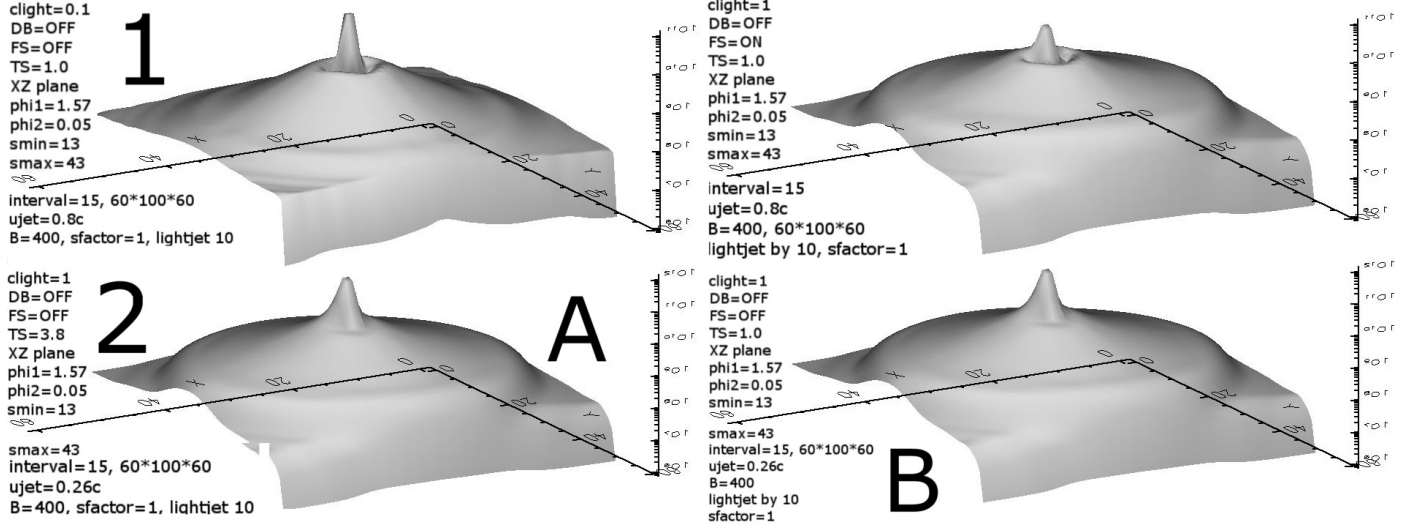


Figure 13: Second part of the third batch of the results.

much smaller differences between the two images, as compared to the previous pair.

#### 4.3. Frequency shift

*A pair.* (process2, page3, 1A, clight=1, ts=1.0, a1=0.005, a2=0.005, DB=yes, FS=no, smin=37, smax=43,  $u_{jet}=0.26c$ , YZ) vs  
 (process2, page3, 2A, clight=1, ts=1.0, a1=0.005, a2=0.005, DB=yes, FS=yes, smin=37, smax=43,  $u_{jet}=0.26c$ , YZ)

Comment: The images look almost the same, with tiny differences found along the jet axis. At such a low jet speed, the  $1/D^2$  effect of FS is limited, resulting to a couple of very similar images.

*A pair.* (process2, page3, 1B, clight=1, ts=3.8, a1=0.005, a2=0.005, DB=yes, FS=no, smin=37, smax=43,  $u_{jet}=0.26c$ , YZ) vs  
 (process2, page3, 2B, clight=1, ts=3.8, a1=0.005, a2=0.005, DB=yes, FS=yes, smin=37, smax=43,  $u_{jet}=0.26c$ , YZ)

Comment: The two images look the same, except along the jet axis. There, the intensity is slightly raised when FS is switched on. At such low angles,

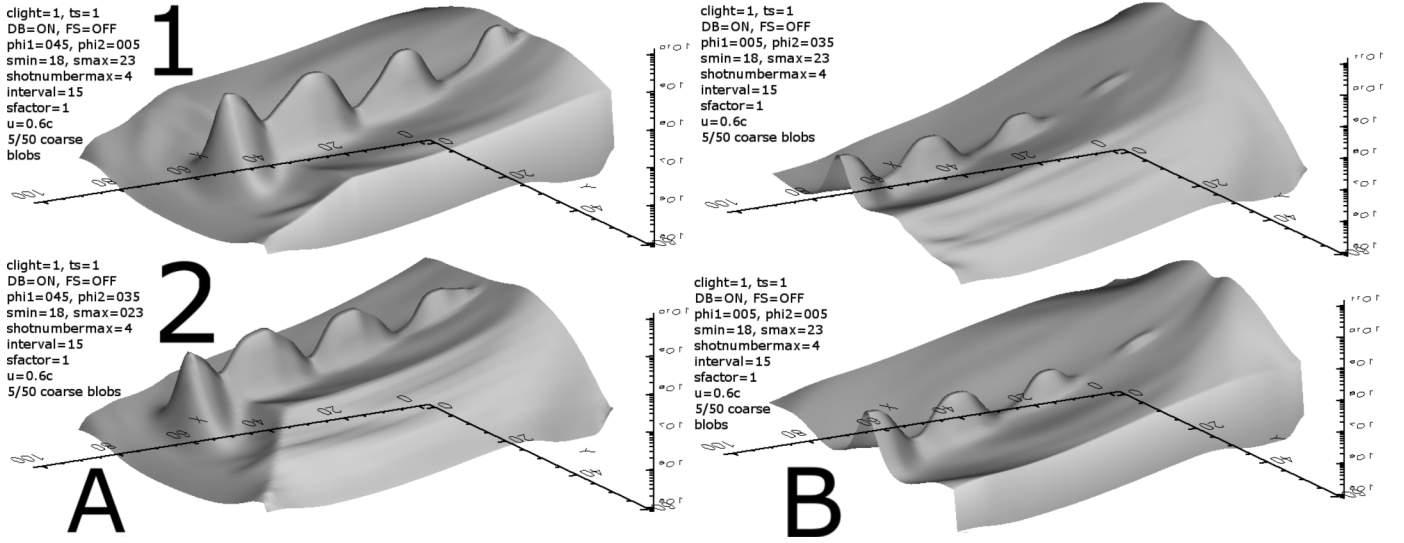


Figure 14: Fourth batch of the results.

the average  $\text{losu}$  is almost  $\pi/2$ , clearly outside the boost cones of most jet axis cells. Combined with such a high effective jet speed ( $ts=3.8$ ), the resulting Doppler factor  $D$  is quite smaller than 1. Consequently, 'losing' two  $D$  factors when FS is turned *on* (Section 2.4.5, case 2 vs case 1) leads to a detectable *increase* in emission along the jet axis. Elsewhere, velocities are lower and the differentiating effect of FS is much weaker.

#### 4.4. Doppler boosting

*A pair.* (process2, page2, 2A, clight=1, ts=3.8, YZ, smin=37, smax=43,  $u_{jet}=0.26c$ ,  $a1=059$ ,  $a2=0.005$ , DB=yes, FS=no) vs

(process3, page1, 1A, clight=1, ts=3.8, YZ, smin=37, smax=43,  $u_{jet}=0.26c$ ,  $a1=059$ ,  $a2=0.005$ , DB=no, FS=no)

Comment: The two images in this pair are quite similar, apart from the jet axis region. On-axis, at such a high effective maximum velocity ( $ts \times c \simeq 0.988$ ), most boost cones are narrow, therefore the angle 1 value of 0.59 rad places the LOS outside them, de-boosting the jet when DB is turned on. Consequently, intensity in this pair is actually higher without DB.



*A pair.* (process2, page2, 2B, clight=1, ts=0.2, YZ, smin=37, smax=43,  $u_{jet}=0.26c$ , a1=0.59, a2=0.005, DB=yes, FS=no) vs  
 (process3, page1, 2B, clight=1, ts=0.2, YZ, smin=37, smax=43,  $u_{jet}=0.26c$ , a1=0.59, a2=0.005, DB=no, FS=no)

390      Comment: These images look very similar, since at such a low ts factor, the effective maximum velocity is  $0.26c \times 0.2 = 0.052c$ , leading to very little relativistic boosting or de-boosting, despite the far from zero value of angle 1.

*A pair.* (process2, page3, 1B, clight=1, ts=3.8, YZ, smin=37, smax=43,  $u_{jet}=0.26c$ , a1=0.005, a2=0.005, DB=no, FS=no) vs  
 395 (process3, page1, 1B, clight=1, ts=3.8, YZ, smin=37, smax=43,  $u_{jet}=0.26c$ , a1=0.005, a2=0.005, DB=no, FS=no)

Comment: Both angles have near zero values, therefore the Doppler-boosted image is much weaker (de-boosting) along the jet axis, at a maximum effective jet speed of  $ts \times 0.26c = 0.988c$ . To the sides, intensities differ much less, due  
 400 to low intrinsic velocities there. The above are attributed to boost cones being narrow enough to exclude from themselves this pair's LOS direction.

*A pair.* (process1, page1, 1A, clight=0.1, ts=1.0, XZ, smin=13, smax=43,  $u_{jet}=0.8c$ , a1=1.57, a2=0.05, DB=yes, FS=no) vs  
 (process3, page2, 1A, clight=0.1, ts=1.0, XZ, smin=13, smax=43,  $u_{jet}=0.8c$ ,  
 405 a1=1.57, a2=0.05, DB=no, FS=no)

Comment: Doppler boosting is quite large in (1, 1, 1A), since angle 1 approaches  $\pi/2$ , lying inside the boost cones of most jet axis cells, at  $u_{jet(injected)}=0.8c$ . When DB is turned on (1, 1, 1A), the jet base footprint appears narrower, limiting the area of stronger emission to the close vicinity of  
 410 the jet axis. The reason is that speed now makes a difference and only the jet axis possesses it. In contrast, deactivating DB largely cancels the above narrowing effect. Furthermore, the 'dark ring' of reduced emission, surrounding the jet axis (3, 2, 1A), represents an area vacated by the winds being pushed away to the sides and is present in the fast jet model run.

415 These images are drawn at low clight (0.1), causing rays to advance at 1/10  
of their normal speed, employing many snapshots, beginning at smin=13. A  
narrower jet projection results, the slower LOS reaching *later* snapshots, when  
winds around the jet base have been pushed away by the jet.

*A pair.* (process1, page1, 2A, clight=1, ts=3.8, XZ, smin=13, smax=43,  
420  $u_{jet}=0.26c$ , a1=1.57, a2=0.05, DB=yes, FS=no) vs  
(process3, page2, 2A, clight=1, ts=3.8, XZ, smin=13, smax=43,  $u_{jet}=0.26c$ ,  
a1=1.57, a2=0.05, DB=no, FS=no)

Comment: A similar case appears here, at a higher ts, where, despite the  
lower clight, the boosted jet looks stronger and narrower, while the de-boosted  
425 one is wider than before. This time the effective jet speed is 0.988c, the result  
of multiplying  $u_{jet}$  and ts.

*A pair.* (process1, page1, 2B, clight=1, ts=1.0, XZ, smin=13, smax=43,  
 $u_{jet}=0.26c$ , a1=1.57, a2=0.05, DB=yes, FS=no) vs  
(process3, page2, 2B, clight=1, ts=1.0, XZ, smin=13, smax=43,  $u_{jet}=0.26c$ ,  
430 a1=1.57, a2=0.05, DB=no, FS=no)

Comment: Employing DB significantly narrows the visible part of the jet  
base, while making it emit somehow stronger as well. On the other hand,  
turning DB off (3, 2, 2B), leads to a wider emission base for the jet, since now  
only density matters to the result.

#### 435 4.5. *Tweak speed*

In this subsection we explore the effects, on the synthetic image, of artificially  
altering, on a global scale, in post-processing, the speed of matter.

*A pair.* (process1, page1, 2A, clight=1, ts=3.8, XZ, smin=13, smax=43,  
 $u_{jet}=0.26c$ , a1=1.57, a2=0.05, DB=yes, FS=no) vs  
440 (process1, page1, 2B, clight=1, ts=1.0, XZ, smin=13, smax=43,  $u_{jet}=0.26c$ ,  
a1=1.57, a2=0.05, DB=yes, FS=no)

Comment: Both images are Doppler boosted. At an effective speed of 0.988c,  
we observe an emission increase by about one hundred times (1, 1, 2A), relative

to the image drawn at the natural speed (1, 1, 2B). The intensity profile, moving  
 445 from the jet periphery radially towards its axis, is steeper, spanning 7 orders of  
 magnitude, for the artificially faster jet, as opposed to only 5 for the normal jet.

*A quartet.* (process2, page2, 1A, clight=1, ts=1.8, YZ, smin=37, smax=43,  
 u<sub>jet</sub>=0.26c, a1=0.59, a2=0.005, DB=yes, FS=no) vs  
 (process2, page2, 1B, clight=1, ts=1.0, YZ, smin=37, smax=43, u<sub>jet</sub>=0.26c,  
 450 a1=0.59, a2=0.005, DB=yes, FS=no) vs  
 (process2, page2, 2A, clight=1, ts=3.8, YZ, smin=37, smax=43, u<sub>jet</sub>=0.26c,  
 a1=0.59, a2=0.005, DB=yes, FS=no) vs  
 (process2, page2, 2B, clight=1, ts=0.2, YZ, smin=37, smax=43, u<sub>jet</sub>=0.26c,  
 a1=0.59, a2=0.005, DB=yes, FS=no)

455 Comment: Given a value of angle 1 of 0.59 rad, Doppler boosting of  $1 \leq D$   
 $\leq 2$  is present along the jet axis at ts = 0.2, 1.0 and 1.8 (maximum effective jet  
 speed of 0.052c, 0.26c and 0.468c respectively). At ts = 3.8 though (0.988c), no  
 boosting occurs along the jet, as boost cones are now too narrow, leaving out  
 losu angles corresponding to angle 1 of .59 rad.

460 *A pair.* (process2, page3, 1A, clight=1, ts=1.0, YZ, smin=37, smax=43,  
 u<sub>jet</sub>=0.26c, a1=0.005, a2=0.005, DB=yes, FS=no) vs  
 (process2, page3, 1B, clight=1, ts=3.8, YZ, smin=37, smax=43, u<sub>jet</sub>=0.26c,  
 a1=0.005, a2=0.005, DB=yes, FS=no)

465 Comment: At an effective speed of 0.988c (2, 3, 1B), boost cones are pretty  
 narrow, therefore at such small angles 1 and 2 as this pair's, the jet axis appears  
 heavily *de*-boosted. On the other hand, at an effective speed of 0.26c (2, 3, 1A)  
 the jet axis still emits significantly, at a representative value of  $D(u \simeq 0.26c,$   
 $\cos\theta \simeq 0) \simeq 0.8$ .

*A pair.* (process2, page3, 2A, clight=1, ts=1.0, YZ, smin=37, smax=43,  
 470 u<sub>jet</sub>=0.26c, a1=0.005, a2=0.005, DB=yes, FS=yes) vs  
 (process2, page3, 2B, clight=1, ts=3.8, YZ, smin=37, smax=43, u<sub>jet</sub>=0.26c,  
 a1=0.005, a2=0.005, DB=yes, FS=yes)

Comment: At high effective velocities, de-boosting occurs, essentially along the jet axis. Compared to the previous pair, Doppler effects are less intense in both images here, being proportional to  $D^{1+\alpha}$ , as opposed to  $D^{3+\alpha}$ .

*A pair.* (process3, page1, 1A, clight=1, ts=3.8, YZ, smin=37, smax=43,  $u_{jet}=0.26c$ , a1=0.59, a2=0.005, DB=no, FS=no) vs  
(process3, page1, 2B, clight=1, ts=0.2, YZ, smin=37, smax=43,  $u_{jet}=0.26c$ , a1=0.59, a2=0.005, DB=no, FS=no)

Comment: Despite a huge difference in effective speeds, no difference occurs, since both DB and FS are turned off. The sole influence left on intensity is matter density, which is identical for both images.

*A pair.* (process3, page2, 2A, clight=1, ts=3.8, XZ, smin=13, smax=43,  $u_{jet}=0.26c$ , a1=1.57, a2=0.05, DB=no, FS=no) vs  
(process3, page2, 2B, clight=1, ts=1.0, XZ, smin=13, smax=43,  $u_{jet}=0.26c$ , a1=1.57, a2=0.05, DB=no, FS=no)

Comment: Both DB and FS are turned *off*, therefore no apparent difference occurs between the two images.

#### 4.6. Clight

Varying clight only affects the LOS's rate of advance, leaving intact the relativistic calculations of Lorentz and Doppler factors.

*A pair.* (process1, page1, 1A, clight=0.1, ts=1.0, XZ, smin=13, smax=43,  $u_{jet}=0.8c$ , a1=1.57, a2=0.05, DB=yes, FS=no) vs  
(process1, page1, 1B, clight=1.0, ts=1.0, XZ, smin=13, smax=43,  $u_{jet}=0.8c$ , a1=1.57, a2=0.05, DB=yes, FS=no)

Comment: We can see here the difference slow-light relativistic imaging (1, 1, 1A) makes, compared to simply imaging at normal light speed (1, 1, 1B). The 'slow' image, formed as a combination of a longer series of snapshots, appears natural to the eye, resembling an intermediate time instant in the jet evolution. The lower the imposed speed of light is (1, 1, 1A), the less laterally developed

the jet emission appears, as later snapshots contribute less to the image (later on, surrounding winds' density, as projected on XZ, around the jet base, tends to fade).

*A quartet.* (process2, page1, 2A, clight=400, ts=1.0, YZ, smin=13, smax=43,  
505  $u_{jet}=0.26c$ , a1=0.005, a2=0.005, DB=yes, FS=no) vs  
(process2, page1, 2B, clight=0.1, ts=1.0, YZ, smin=13, smax=43,  $u_{jet}=0.26c$ ,  
a1=0.005, a2=0.005, DB=yes, FS=no) vs  
(process2, page1, 1A, clight=400, ts=1.0, YZ, smin=31, smax=43,  $u_{jet}=0.26c$ ,  
a1=0.005, a2=0.005, DB=yes, FS=no) vs  
510 (process2, page1, 1B, clight=400, ts=1.0, YZ, smin=42, smax=43,  $u_{jet}=0.26c$ ,  
a1=0.005, a2=0.005, DB=yes, FS=no)

Comment: The result of slowing down light, by 10 times (2, 1, 2B), is compared to three effectively single shot images (clight = 400), taken at different time instants (smin  $\times$  interval = smin  $\times$  15). The jet traverses a substantial  
515 portion of the computational grid during the formation of the 'slow light' synthetic image, as compared to the earliest snapshot of this group (2, 1, 2A). (2, 1, 2B) appears quite natural to the eye, resembling an intermediate snapshot, between (2, 1, 1A) and (2, 1, 1B).

## 5. Conclusions

520 RLOS has evolved from its classical ancestor LOS code, in order to address the problem of imaging model *relativistic* astrophysical jets. Despite its theoretical simplifications, the program succeeds in providing a time-delayed synthetic image of a hydrodynamical model jet, while avoiding the complexity of a more complete approach. Applications may include a variety of dynamical astrophys-  
525 ical phenomena, where synthetic observations are compared to actual ones, an achieved match largely validating the initial conditions of the numerical models.

RLOS tests verify the integrity of the program and demonstrate its versatility, when imaging a model astrophysical system. We also note its ability to incorporate various emission and absorption coefficients, covering different

530 wavebands, from radio to  $\gamma$ -rays. What's more, the use of a hydrocode allows  
modelling complex dynamical systems, facilitating the study of many scenarios.

Furthermore, apart from the currently employed dependence on density,  
emission may also be a function of the magnetic field, local velocity, and others.  
An example is X-ray synchrotron radiation, which also includes a direct de-  
535 pendence on the frequency shift effect. Certain particle emissions may even be  
modelled, if suitable directional relativistic expressions are employed, transform-  
ing emission from the jet to the stationary frames of reference. The inclusion  
of aberration is a potential next step in the program development, along with  
certain gravitational corrections to the ray path.

## 540 References

- [1] A. Lampa, Zeitschrift fur Physik 27 (1924) 138.
- [2] J. Terrell, Phys. Rev. 116 (1959) 1041.
- [3] R. Penrose, Proc. Cambridge Phil. Soc. 55 (1959) 137.
- [4] V. F. Weisskopf, Phys. Today 13 (1960) 24.
- 545 [5] G. D. Scott, M. R. Viner, American Journal of Physics 33 (1965) 534.
- [6] D. Weiskopf, Dissertation, Ph.D. thesis, Dissertation, der Eberhard-Karls-  
Universitat zu Tubingen, der Fakultat fur Physik (2001).
- [7] R. J. Deissler, Am. J. Phys. 73 (2005) 663.
- [8] D. Weiskopf, in: H. Hagen (Ed.), Scientific Visualization: Advanced Con-  
550 cepts, Dagstuhl Publishing, Leibniz Center for Informatics, Germany, 2010,  
p. 289302.
- [9] I. F. Mirabel, L. F. Rodríguez, Ann. Rev. Astron. Astrophys. 37 (1999) 409.
- [10] T. V. Cawthorne, in: Hughes (Ed.), Beams and Jets in Astrophysics, Cam-  
bridge University Press, 1991.

- 555 [11] P. A. Hughes, in: Hughes (Ed.), *Beams and Jets in Astrophysics*, Cambridge University Press, 1991.
- [12] D. Weiskopf, U. Kraus, H. Ruder, *ACM Trans. Graph.* 18 (1999) 3.
- [13] R. D. Klauber, Is detection of fitzgerald-lorentz contraction possible?, arXiv:0808.1117v1 (2008).
- 560 [14] G. B. Rybicki, A. P. Lightman, *Radiative Processes in Astrophysics*, Wiley-Interscience, New York, 1979.
- [15] A. Jarabo, B. Masia, A. Velten, C. Barsi, R. Raskar, D. Gutierrez, *Computer Graphics Forum*, 34 (8) 34 (2015) 1.
- [16] F. R. Hickey, *Am. J. Phys.* 47 (1979) 711.
- 565 [17] P. Hsiung, R. Dunn, *Proceedings of Supercomputing 1989 Conference* 1 (1989) 597.
- [18] P. Hsiung, R. Thibadeau, M. Wu, *Computer Graphics* 24(2) 24 (1990) 83.
- [19] U. Kraus, *American Journal of Physics* 68 (2000) 56.
- [20] T. Muller, S. Boblest, *Eur. J. Phys.* 35 (2014) 06502.
- 570 [21] T. Muller, *Comput. Phys. Commun.* 185 (2014) 2301.
- [22] A. Velten, D. Wu, A. Jarabo, B. Masia, C. Barsi, C. Joshi, E. Lawson, M. Bawendi, D. Gutierrez, R. Raskar, *ACM Trans. Graph.* 32 (2013) 4.
- [23] Z. W. Sherin, R. Cheu, P. Tan, G. Kortemeyer, Visualizing relativity: the openrelativity project, *American Journal of Physics* 84 (2016) 369.
- 575 [24] T. Smponias, T. S. Kosmas, *MNRAS* 412 (2011) 1320.
- [25] T. Smponias, T. S. Kosmas, *MNRAS* 438 (2014) 1014.
- [26] O. Kosmas, T. Smponias, *aHEP* accepted (2018).
- [27] R. M. Hjellming, K. J. Johnston, *ApJ* 328 (1988) 600.

- [28] A. Mignone, G. Bodo, S. Massaglia, T. Matsakos, O. Tesileanu, C. Zanni,  
580 A. Ferrari, *Ap. J. Supp.*170 (2007) 228.
- [29] W. B. Sparks, D. Fraix-Burnet, F. Macchetto, F. N. Owen, A counterjet  
in the elliptical galaxy m87, *Nature* 355 (1992) 804.
- [30] R. Laing, A. H. Bridle, Relativistic models and the jet velocity field in the  
radio galaxy 3c 31, *Monthly Notices of the Royal Astronomical Society* 336  
585 (2002) 328.
- [31] G. Kortemeyer, P. Tan, S. Schirra, A slower speed of light: Developing  
intuition about special relativity with games fdg 2013, *FDG 13 Proceedings  
of the International Conference on the Foundations of Digital Games. ACM  
New York, NY, USA* 1 (2013) 400.
- 590 [32] T. Smponias, O. Kosmas, *Advances in High Energy Physics* 921757.
- [33] T. Smponias, O. Kosmas, *Advances in High Energy Physics* 4962741.